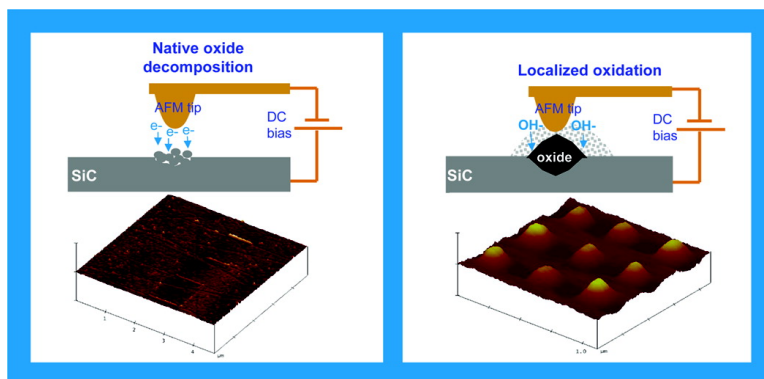Article

Probe-Induced Native Oxide Decomposition and Localized Oxidation on 6H-SiC (0001) Surface: An Atomic Force Microscopy Investigation

Xian Ning Xie, Hong Jing Chung, Hai Xu, Xin Xu, Chorng Haur Sow, and Andrew Thye Shen Wee

More About This Article

Additional resources and features associated with this article are available within the HTML version:

- Supporting Information
- Links to the 2 articles that cite this article, as of the time of this article download
- Access to high resolution figures
- Links to articles and content related to this article
- Copyright permission to reproduce figures and/or text from this article

View the Full Text HTML

Probe-Induced Native Oxide Decomposition and Localized Oxidation on 6H-SiC (0001) Surface: An Atomic Force Microscopy Investigation

Xian Ning Xie,[†] Hong Jing Chung,[†,‡] Hai Xu,[‡] Xin Xu,[§] Chorng Haur Sow,[†,‡] and Andrew Thye Shen Wee*,[†,‡]

Contribution from the NUS Nanoscience & Nanotechnology Initiative, National University of Singapore, 2 Science Drive 3, Singapore, 117542, Department of Physics, National University of Singapore, 2 Science Drive 3, Singapore, 117542, and Temasek Laboratories, National University of Singapore, Engineering Drive 2, Singapore, 119260

Received January 25, 2004; E-mail: phyweets@nus.edu.sg

Abstract: We report, for the first time, the native oxide decomposition/etching and direct local oxide growth on 6H-SiC (0001) surface induced by atomic force microscopy (AFM). Surface native oxide was decomposed and assembled into protruded lines when the negatively biased AFM tip was scanned over surface areas. The mechanism of decomposition was found to be governed by the Fowler-Nordheim emission current enhanced by the negatively biased AFM tip. Direct oxide growth on the SiC surface was achieved when the AFM tip was immobilized and longer bias duration applied. In particular, the aspect ratio of oxide grown on SiC was found to be several times higher than that on the Si surface. The improved aspect ratio on SiC was attributed to the anisotropic OH^- diffusion involved in vertical and lateral oxidation along the polar and nonpolar directions such as [0001] and [11$\bar{2}$0] axis in SiC crystal. The electron transport in the above AFM grown oxide on SiC was further investigated by $I-V$ characteristics. The dielectrical strength of AFM oxide against degradation and breakdown under electrical stressing was evaluated.

Introduction

Silicon carbide (SiC) is a wide band gap semiconductor which exhibits high breakdown field, good thermal conductivity, and chemical inertness.[1] For the hexagonal 6H-SiC polytype, the energy band gap and breakdown field are 3.0 eV and 3.2 MV/cm, respectively.[2] The melting point of 6H-SiC is as high as 1800 °C. Thus, SiC is advantageous over Si for high power, high frequency, and high temperature applications. Moreover, SiC is the only compound semiconductor on which oxide can be thermally grown for metal oxide semiconductor (MOS) device fabrication.[3,4] In the MOS processing, the SiC substrate is first oxidized in wet or dry oxygen at temperatures above 1050 °C. Then, metal gates are deposited, and photolithography and wet etching are applied to define a MOS structure. The dielectric properties of thermally grown oxide have been studied using capacitance-voltage ($C-V$) and current-voltage ($I-V$) measurements on the above MOS structure.[5-7] The barrier

height, ϕ, for the thermally grown SiO_2/SiC interface was determined to be in the range of 2.2-3.1 eV, depending on the SiC crystal orientation and quality of thermal oxide.[2,7,8]

Atomic force microscopy (AFM) based nanolithography has wide applications in nanoscale patterning and fabrication. So far, dip-pen (DPN),[9-12] local anodic oxidation,[13-20] and other related techniques[21-23] have been developed to selectively modify a surface and build up complex nanostructures. For example, AFM could be used to directly transfer molecules to a surface,[9-12] to selectively scratch self-assembled monolayers, etc.[21-23] The cutting of multiwalled carbon nanotubes and etching of graphite via field emitted current injection from an

† NUS Nanoscience & Nanotechnology Initiative.
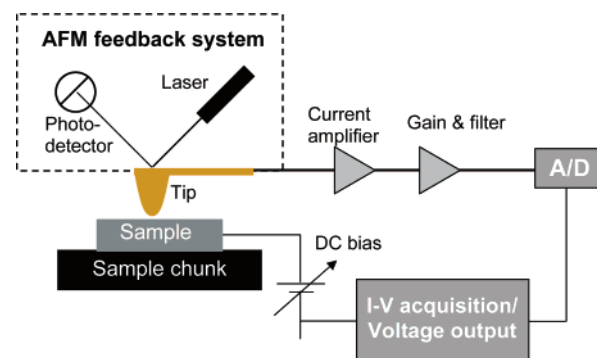‡ Department of Physics.
§ Temasek Laboratories.
(1) Neudeck, P. G. *J. Electron Mater.* **1995**, *24*, 283.
(2) Shenoy, J. N.; Das, M. K.; Cooper, J. A., Jr.; Melloch, M. R. *J. Appl. Phys.* **1996**, *79*, 3042.
(3) Xie, W.; Cooper, J. A., Jr.; Melloch, M. R. *IEEE Trans. Electron Device Lett.* **1994**, *15*, 455.
(4) Chang, K. C.; Nuhfer, N. T.; Porter, L. M.; Wahab, Q. *Appl. Phys. Lett.* **2000**, *77*, 2186.
(5) Yano, H.; Kimoto, T.; Matsunami, H. *Appl. Phys. Lett.* **2002**, *81*, 301.
(6) Yano, H.; Hirao, T.; Kimoto, T.; Matsunami, H. *Appl. Phys. Lett.* **2001**, *78*, 374.
(7) Friedrichs, P.; Burte, E. P.; Schörner, R. *Appl. Phys. Lett.* **1994**, *65*, 1665.
(8) Alok, D.; McLarty, P. K.; Baliga, B. J. *Appl. Phys. Lett.* **1994**, *65*, 2177.
(9) Piner, R. D.; Zhu, J.; Xu, F.; Hong, S.; Mirkin, C. A. *Science* **1999**, *283*, 661.
(10) Hong, S.; Zhu, J.; Mirkin, C. A. *Science* **1999**, *286*, 523.
(11) Ivanisevic, A.; Mirkin, C. A. *J. Am. Chem. Soc.* **2001**, *123*, 7887.
(12) Agarwal, G.; Sowards, L. A.; Naik, R. R.; Stone, M. O. *J. Am. Chem. Soc.* **2003**, *125*, 580.
(13) Gordon, A. E.; Fayfield, R. T.; Litfin, D. D.; Higman, T. K. *J. Vac. Sci. Technol. B* **1995**, *13*, 2805.
(14) Snow, E. S.; Campbell, P. M. *Appl. Phys. Lett.* **1994**, *64*, 1932.
(15) Legrand, B.; Stievenard, D. *Appl. Phys. Lett.* **1999**, *74*, 4049.
(16) Ph. Avouris, Hertel, T.; Martel, R. *Appl. Phys. Lett.* **1997**, *71*, 285.
(17) Snow, E. S.; Jernigan, G. G.; Campbell, P. M. *Appl. Phys. Lett.* **2000**, *76*, 1782.
(18) Dtievenard, D.; Fontaine, P. A.; Dubois, E. *Appl. Phys. Lett.* **1997**, *70*, 3272.
(19) Dagata, J. A.; Inoue, T.; Yokoyama, H. *Appl. Phys. Lett.* **1998**, *73*, 271.
(20) Dagata, J. A.; Perez-Murano, F.; Abadal, G.; Morimoto, K.; Inoue, T.; Itoh, J.; Yokoyama, H. *Appl. Phys. Lett.* **2000**, *76*, 2710.
(21) Wacaser, B. A.; Maughan, M. J.; Mowat, I. A.; Niederhauser, T. L.; Linford, M. R.; Davis, R. C. *Appl. Phys. Lett.* **2003**, *82*, 808.
(22) Lee, H.; Kim, S. A.; Ahn, S. J.; Lee, H. *Appl. Phys. Lett.* **2002**, *81*, 138.
(23) Ahn, S. J.; Jang, Y. K.; Lee, H.; Lee, H. *Appl. Phys. Lett.* **2002**, *80*, 2592.

AFM tip was also demonstrated recently.[24] In the local anodic oxidation (AFM oxidation), the negatively biased tip induces simultaneous oxide growth on conductive surfaces. It is suggested that the oxidation mechanism and kinetics are closely related to electrical field, surface stress, water meniscus, and OH^- diffusion etc.[13-20] Ultrathin oxide patterns (thickness ≤ 5.0 nm) with line width down to tens of nanometers have been fabricated on a Si surface using AFM oxidation.[16-18] Besides being a powerful fabrication tool to grow oxide, AFM is also a good technique to determine the local conduction and dielectrical properties of oxide grown.[25-27] By integrating a current sensor into the AFM system, the $I-V$ characteristics of the oxide could be measured in the so-called conducting AFM (c-AFM) setup. The c-AFM is more feasible in electrical characterization compared to other techniques such as scanning tunneling microscopy (STM), ballistics electron emission microscopy (BEEM), and scanning capacitance microscopy (SCM) in terms of experimental setup, ease of operation, and measurement resolution.[25] The high lateral resolution (~10 nm), extreme vertical sensitivity (<0.1 nm) of AFM, and its easy operation in ambient condition makes c-AFM promising in nanoscale $I-V$ characterization. This is especially true in the case of characterizing AFM oxide which is usually several nanometers thick. In addition to $I-V$ measurements, both the morphology and current mapping of the surface can be acquired in parallel using c-AFM.[25,26]

Although AFM oxidation has been successfully applied on Si,[13-20] metallic and dielectrical films,[28,29] so far there has been no report of the AFM oxidation of SiC, despite the fact that SiC is a IV-IV compound semiconductor with properties that are desired more. The oxidation of SiC is crucial to the fabrication of SiC-based micro/nano electrical devices. Various chemicals approaches such as gas phase thermal oxidation,[3,4] $HClO_4$ wet oxidation,[30] and TiO_2 photocatalysis oxidation[31] have been attempted for SiC oxidation. The thermal oxidation requires high-temperature annealing and multiple-step treatments.[3,4] The wet oxidation needs longer oxidation time and post-oxidation annealing.[30] The TiO_2 photocatalysis oxidation can be carried out in dry conditions at room temperature, but the lateral resolution of the oxide pattern is limited.[31] Thus, it is desirable to explore an alternative SiC oxidation approach which is suitable to generating nanoscale oxide patterns at low temperature. AFM oxidation is usually conducted at room temperature in air. The dimension of oxide patterns can be precisely controlled by optimizing conditions such as tip voltage and oxidation time.[16-18] Furthermore, the oxide dielectrical behavior could also be examined by c-AFM in situ immediately after oxidation. Motivated by the above factors, we investigated the oxidation of 6H-SiC (0001) surface using AFM probe oxidation. In this paper, we present a comparative study of the oxidation of SiC and Si semiconductors by AFM. We observed (1) AFM induced native oxide decomposition/reassembling and (2) direct

(24) Kim, D.-H.; Koo, J.-Y.; Kim, J.-J. *Phys. Rev. B* **2003**, *68*, 113406.
(25) Olbrich, A.; Ebersberger, B.; Boit, C. *Appl. Phys. Lett.* **1998**, *73*, 3114.
(26) Porti, M.; Nafría, M.; Aymerich, X. *Appl. Phys. Lett.* **1998**, *73*, 3114.
(27) Blasco, X.; Nafría, M.; Aymerich, X. *Surf. Sci.* **2003**, *532–535*, 732.
(28) F. Chien, S.-S.; Chou, Y. C.; Chen, T. T.; Hsieh, W.-F.; Chao, T.-S.; Gwo, S. *J. Appl. Phys.* **2001**, *89*, 2465.
(29) Cooper, E. B.; Manalis, S. R.; Fang, H.; Dai, H.; Matsumoto, K.; Minne, S. C.; Hunt, T.; Quate, C. F. *Appl. Phys. Lett.* **1999**, *75*, 3566.
(30) Sakurai, T.; Nishiyama, M.; Nishioka, Y.; Kobayashi, H. *Appl. Phys. Lett.* **2002**, *81*, 271.
(31) Ishikawa, Y.; Matsumoto, Y.; Nishida, Y.; Taniguchi, S.; Watanabe, J. *J. Am. Chem. Soc.* **2003**, *125*, 6558.

Figure 1. Experimental setup of conducting atomic force microscopy (c-AFM) for $I-V$ characteristic measurements.

local oxidation on SiC (0001) surface in two different oxidation approaches. The former took place when the biased AFM tip was scanned over a surface region, and the latter was achieved when the tip was immobilized at a surface position for longer oxidation time. A higher aspect ratio of AFM oxide was obtained on SiC compared to the Si surface. The dielectrical properties of AFM oxide grown were also investigated in terms of interface barrier height, degradation, and breakdown.
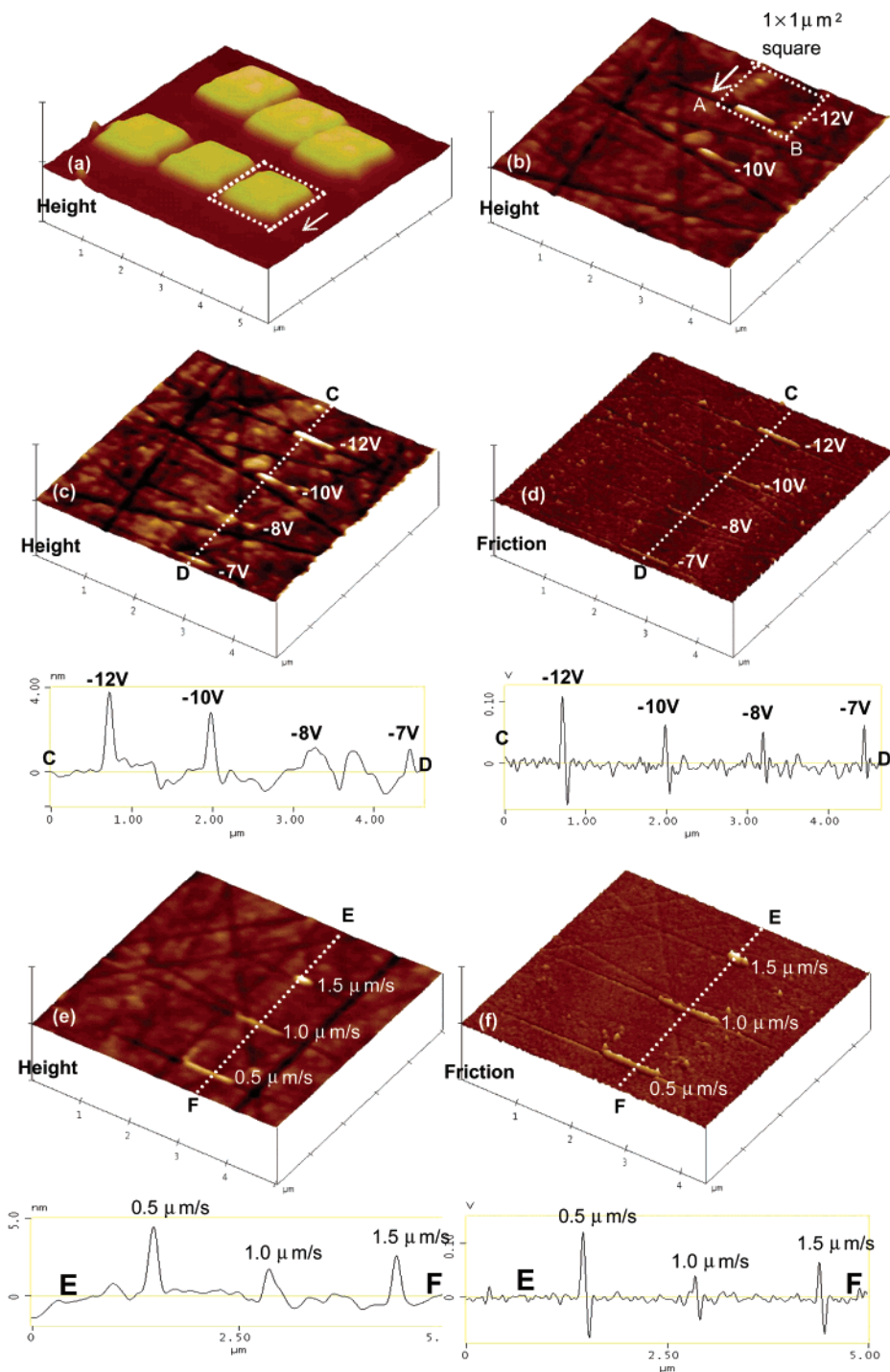
Experimental Section

N-type 6H-SiC (on-axis, resistivity: 0.02–0.20 Ohm-cm, Cree Inc.) were ultrasonically cleaned in acetone and blown dry in N_2. The samples were then subjected to AFM oxidation and measurement under ambient conditions. Two approaches were applied for the oxidation. In the first case, the negatively biased AFM tip was scanned across certain areas, e.g., 1×1 μm^2 squares with 0.2–1.5 Hz scan rates to grow oxide islands on SiC. In the second approach, the tip was immobilized at a fixed position, and negative tip biases with long durations (0.5–2.0 s) were applied to grow oxide dots. All $I-V$ curve measurements were conducted on oxide using a c-AFM setup as shown in Figure 1 where the conductive AFM tip was effectively the metal electrode of the MOS structure. A current sensor with the sensitivity from fA to μA range was used. During $I-V$ measurements, the AFM tip was kept in contact with the surface, and the current was recorded by ramping the tip voltage in the range of 0–12 V. Positive tip voltage was used to avoid possible surface oxidation in $I-V$ curve collection. A NanoMan AFM system (Veeco Instruments & Process Metrology) was employed for all AFM experiments. Au-coated Si_3N_4 contact tips were used in the oxidation and measurement of $I-V$ characteristics. For comparison, the same AFM oxidation procedures were also carried out on Si (111) samples. All the AFM experiments were conducted under an ambient humidity of ~75%, unless otherwise specified in the text.

Results and Discussion

I. Native Oxide Decomposition on 6H-SiC (0001). Figure 2a shows six oxide islands (~2 nm thick, 1×1 μm^2) grown on the Si surface by scanning a negatively biased AFM tip (bias voltage 12 V) across 1×1 μm^2 areas. It is observed that oxidation occurs simultaneously as the tip scans over the surface. In contrast, when the same procedures were applied to the SiC (0001) surface, no oxidation was detected. Instead, a protruded line (AB line for example, height ~4 nm) was generated at the end edge of the scanned area as shown in Figure 2b. When a lower magnitude of bias voltage was used in the scan, protruding lines with reduced line height were always formed at the end side. Figures 2c and 2d display the height and friction images of four lines generated sequentially with 12, 10, 8, and 7 V negative tip bias. The tip scanning rate also influences the

Figure 2. (a) Six $1 \times 1\ \mu m^2$ oxide squares grown on Si. (b) Protruded lines (e.g., AB line) generated by scanning $1 \times 1\ \mu m^2$ area on SiC with different tip bias. (c) and (d) Height and friction images of four lines fabricated at various tip bias. (e) and (f) Height and friction images of three lines formed by scanning $1 \times 1\ \mu m^2$ areas at different scan rates.

formation of lines. As shown in Figures 2e and 2f, a lower scan rate (e.g., 0.5 μm/s) favors uniform line formation, while a higher scan rate (e.g., 1.5 μm/s) leads to a shorter line. It is also noted that the line assembled at 1.5 μm/s scan rate in Figure 2e is slightly taller than the one made at 1.0 μm/s scan rate. This might be due to (i) the faster scan rate, which causes the decomposition to be more localized at the central region of the $1 \times 1\ \mu m^2$ area; (ii) possible formation of silicon oxycarbide, which gives rise to a change in the density of assembled oxide. For all the above AFM lithographic experiments on SiC, a constant force set-point of 100 nN was used. From Figure 2,

we see that under identical conditions AFM oxidation takes place on Si, but not SiC. Such differences in Si and SiC oxidation could be due to the higher binding energy of the Si−C bond (451.5 kJ/mol) compared to that of Si−Si bond (325 kJ/mol).[32] The chemical inertness and low diffusion coefficients of oxidative species in SiC[2,33] would hinder oxide growth on SiC in this approach. As with the AFM oxidation of Si$_3$N$_4$ films

(32) Lide, D. R., Editor-in-Chief. *CRC Handbook of Chemistry and Physics*, 84th ed., 2003−2004, CRC Press: Boca Raton, FL, 2003.
(33) Negoro, Y.; Miyamoto, N.; Kimoto, T.; Matsunami, H. *Appl. Phys. Lett.* **2002**, *80*, 240.
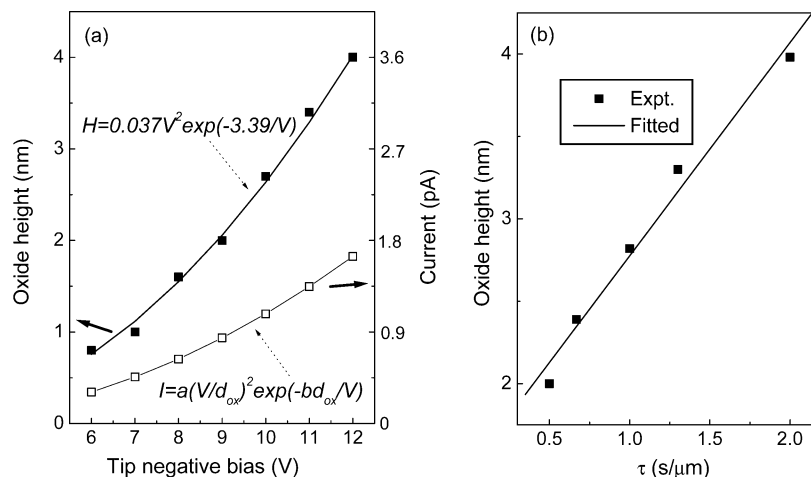
Figure 3. (a) Plots of *H* and *I* curves based on eqs 1 and 2 without scaling factor α. After introducing α, the mismatch between *H* and *I* curves is only 5.4%. (b) Variation of oxide height as a function of τ, the reciprocal of scan rate.

where a higher voltage is needed to completely convert Si_3N_4 to SiO_2,[34,35] the presence of C atoms in the SiC compound and its removal as CO or CO_2 species also implies that extra activation energy is needed for the oxidation of SiC.[36] Indeed, a rate 10 times slower has been reported for the thermal oxidation of SiC as compared to Si.[37] Since no oxide growth is observed in the scanned areas in Figure 2b−f, we ascribe the protruding lines to the assembly of decomposed native oxide on SiC: during the AFM scanning, the electrical field induces the decomposition of native oxide. The debris of native oxide is pushed along the scan direction and piled up at the end edge where the tip stops scanning. The chemical content of the lines was assigned to native oxide because the lines could be preferentially etched in dilute HF solution. Further, such decomposition was not observed on a graphitized or H-plasma cleaned SiC surface which is free of native oxide. Here, the scanning of the biased AFM tip induces oxide growth on Si but native oxide decomposition on SiC. In principle, the native oxide on Si should be more prone to decomposition as compared to that on SiC: the native oxide on Si can be removed by either wet etching or thermal annealing in a UHV chamber,[38] while that on SiC cannot be completely removed using the same procedures. Dosing of additional Si and subsequent annealing in UHV is required to fully desorb the native oxide on a SiC surface.[39,40] It might be possible that both oxide growth and native oxide decomposition coexist on Si. The latter was not observed probably because the former is the predominant process under our experimental conditions. In addition, the products of oxide decomposition on Si are usually SiO and SiO_2 volatile species; these products can easily vaporize, leaving little or no residual on the surface.

From Figure 2b−f, we see that when the negatively biased tip scans across the surface areas, the native oxide was decomposed and pushed, assembled into lines. Such oxide decomposition was not observed when the tip bias was converted to a positive polarity. We also notice a general trend that higher tip voltage corresponds to higher oxide line height. This seems to imply that the energy for the native oxide decomposition/ etching is closely related to the field emission electrons from the AFM tip. In the applied voltage range, the strength of the electrical field already reaches 10^9−10^{10} V/m, which is high enough for field emission.[24] In Figure 3a, we plot the variation of native oxide line height as a function of tip bias. The line height (*H*) can be best described by the following equation:

$$H = 0.037V^2 \exp(-3.39/V) \qquad (1)$$

Here, *V* is the magnitude of tip negative bias and 0.037 and −3.39 are the best-fit parameters. This equation is essentially analogous to the Fowler-Nordheim (F-N) equation:[24]

$$I = aE^2 \exp(-b/E) \qquad (2)$$

where *I* and *E* are the current and electrical field. The parameters *a* and *b* are defined as:

$$a = A_{eff}\frac{q^2 m_0}{8\pi h m_{eff}}\frac{1}{t(E)^2}\frac{\beta^2}{\phi} \qquad (3)$$

$$b = \frac{8\pi\sqrt{2qm_{eff}}}{3h\beta}v(E)\phi^{3/2} \qquad (4)$$

in which *q* is the electron charge, *h* the Plank constant, m_{eff}/m_0 the normalized effective mass of electrons in the conduction band of oxide, A_{eff} the effective area, β the field enhancement factor, and φ the barrier height, with the *t(E)* and *v(E)* functions accounting for the image charge lowering effects. By comparing the *H* values derived from eq 1 to the *I* values calculated from eq 2, we found that there is not only a good similarity in the exponential format between eqs 1 and 2, but also a proportional relation between *H* and *I* values for certain *a*, *b* parameters. That is, *H* and *I* are correlated by a scaling factor, α, if suitable *a* and *b* parameters are chosen. This further implies that the decomposition could be induced by the F-N current, and the scaling between *H* and *I* may arise due to the efficiency in energy conversion and oxide packing. In our calculation of *I*

(34) Klauser, R.; Hong, I.-H.; Su, H.-J.; Chen, T. T.; Gwo, S.; Wang, S.-C.; Chuang, T. J.; Gritsenko, V. A. *Appl. Phys. Lett.* **2001**, *79*, 3143.
(35) Gwo, S.; Wu, C.-L.; F. Chien, S.-S.; Yasuda, T.; Yamasaki, S. *Jpn. J. Appl. Phys.* **2001**, *40*, 4368.
(36) Buckzo, R.; Pennycook, S.; Pantelides, S. T. *Phys. Rev. Lett.* **2000**, *84*, 943.
(37) Vickridge, I. C.; Trimaille, I.; Ganem, J.-J.; Rigo, S.; Radtke, C.; Baumvol, I. J.; Stedile, F. C. *Phys. Rev. Lett.* **2002**, *89*, 256102.
(38) Cao, X. P.; Hamers, R. J. *J. Am. Chem. Soc.* **2001**, *123*, 10988.
(39) Chen, W.; Loh, K. P.; Xu, H.; Wee, A. T. S. *Appl. Phys. Lett.* **2004**, *84*, 281.
(40) Xie, X. N.; Wang, H. Q.; Wee, A. T. S.; Loh, K. P. *Surf. Sci.* **2001**, *478*, 57.

Table 1. Typical Variables of Interface Barrier Height, ϕ, Field Enhancement Factor, β, and Scaling Factor, α, Used in the F-N Fitting

SiC/SiO$_2$ interface barrier height, ϕ (eV)	field enhancement factor, β	scaling factor, α	minimum mismatch between H and αI
2.2	5	16.7	14.1%
	10	**2.9**	**8.3%**
	20	0.62	12.0%
2.6	5	18.4	15.7%
	10	**2.2**	**5.4%**
	20	0.48	10.3%
3.0	5	17.3	16.3%
	10	**2.8**	**7.6%**
	20	0.51	11.7%

values, $m_{eff}/m_0 = 0.42$ was taken for electrons in the SiC surface oxide.[7] The value of A_{eff} is related to the tip/surface contacting area which is dependent on the applied force on the tip. We assumed a typical value of $A_{eff} = 100$ nm^2, which corresponds to the force range applied in our AFM nanolithography.[41,42] The values of $t(E)$ and $v(E)$ were assumed to be ~0.93 and ~1.0, respectively,[41] for the electrical field range used in our AFM experiments. The interface barrier height, ϕ, and field enhancement factor, β, were varied to acquire reasonable I values. Interestingly, by setting $H = \alpha I$, we could derive meaningful ϕ and β parameters from eq 2. As shown in Table 1, when $\alpha = 2.2$, we obtained $\phi = 2.6$ eV and $\beta = 10$, for which the mismatch between H and αI is as low as 5.4%. The value of $\phi = 2.6$ eV is lower than that of 2.95 eV reported for thermal oxide on the 6H-SiC (0001) surface.[7] This lower value is reasonable as the oxide considered here is native oxide. Figure 3a shows the plots of H–V and I–V before introducing the scaling factor. The curve of I is based on the best fit parameters of $\phi = 2.6$ eV and $\beta = 10$ and is plotted by converting E to V via $E = V/d_{ox}$ (assuming $d_{ox} = 1.5$ nm). It is clear that the H and I curves follow a similar V dependence throughout the voltage range. After introducing a factor of $\alpha = 2.2$, the H and I curves almost overlap completely with a lowest mismatch of 5.4%. It is remarkable to note that β significantly affects the fitting between H and I. For all the values of ϕ considered in the range 2.2–3.2 eV, a best fit was inevitably obtained at $\beta = 10$. When lower or higher β values were used, e.g., $\beta = 5$ or $\beta = 20$, the fitting mismatch increased dramatically as shown in Table 1. It has been suggested that for AFM experiments involving tip induced field, values of $\beta > 1$ must be considered to account for the field enhancement arising from the nonplanar geometry of the tip.[25,41] The parameter of $\beta = 10$ obtained here is quite reasonable considering the typical tip radius (20–50 nm) and the thickness of native oxide (1–2 nm). When the tip is negatively biased, electrons are directly injected from the tip to the surface. Due to the field enhancement effect of the sharp tip, the electron density would be much higher than that available at a positive tip bias. In the case of a positive tip bias, electrons are emitted from the flat surface instead. This explains why native oxide decomposition was only observed at a negative tip bias. The polarity dependence of oxide decomposition most probably originates from the different field enhancement effects between negative and positive tip bias. Indeed, dramatic field enhancement (with $\beta = 470$) has been reported for nanoscale

filament-like graphite in carbon thin films.[43] Recently, the etching of graphite and cutting of carbon nanotubes were also attributed to the F-N current enhanced by a negatively biased AFM tip.[24] Here, our F-N based analysis not only provides a good numerical match between H and I, but also reveals the physical origin of the decomposition phenomenon. This brings us a degree of confidence that the F-N emission best describes the tip induced native oxide decomposition. Basically, the electrons emitted from the negatively biased tip supplies the energy for the decomposition and assembly of native oxide on SiC. The exponential growth of H with increasing V would bring about the increased degree of decomposition, and thus the increased line height. The polarity dependence of decomposition could be due to the stronger field enhancement available at negative tip bias. Only the electrons injected from the AFM tip can get high enough energy above a certain threshold to decompose the native oxide. Besides tip bias, the scan rate also influences the assembly of decomposed native oxide. As shown in Figure 3b, the height of assembled oxide changes linearly as a function of the reciprocal of scan rate, τ. A slower scan rate allows more injecting electrons at one surface position, thus enhancing the decomposition process and facilitating high and uniform lines assembled at the edge. On the other hand, the assembly of decomposed oxide species is worse when the scan rate is too fast as in the case of 1.5 μm/s shown in Figure 2e.

II. Local Oxide Growth on 6H-SiC (0001). To directly grow oxide on SiC, we attempted another method whereby the tip was immobilized and the negative tip bias was kept for prolonged time durations. In this approach, the oxide dot was directly grown on SiC (0001) surface as shown in Figure 4. In Figure 4a, three oxide dots, R, S, and T, were generated with 12, 8, and 6 V negative tip bias. Figure 4b shows three oxide dots, U, V, and W, grown under the same bias, but at different bias durations. Figure 4c displays a 3 × 3 array of oxide dots grown on a SiC surface using similar conditions. Here, the direct growth of oxide is achieved due to the much longer oxidation time available in this approach. The typical bias duration (oxidation time) at one fixed surface point is 0.5–2.0 s. This oxidation time is at least ~1000 times longer than that used above by scanning the tip across 1 × 1 μm^2 areas. In the first approach, the time in which the biased tip stays at one pixel position is only ~2 × 10^{-3} s for a scan rate of 0.5 Hz. For such a short time, the field only induces native oxide decomposition as observed in Figure 2. In the second approach, by immobilizing the tip and increasing the oxidation time by 3 orders of magnitude, the direct growth of oxide on the SiC surface can be achieved. Figures 4d and 4e display the variation in oxide height as a function of tip negative bias and bias durations, respectively. For all bias durations, oxidation of SiC is observable above 5 V. The oxide height shows exponential growth and saturates at prolonged oxidation time (see Figure 4e). This self-limiting time dependence differs from the kinetics derived from the Cabrera-Mott assumption[13,16,18] but is quite consistent with the Alberty-Miller model proposed for AFM oxidation of Si surfaces.[20] The increasing oxide height, buildup of stress and space charge are responsible for the rapid decay in growth rate observed for longer bias durations. In a comparative study, oxide dots were grown on both SiC and Si

(41) O'Shea, S. J.; Atta, R. M.; Murrell, M. P.; Welland, M. E. *J. Vac. Sci. Technol. B* **1995**, *13*, 1945.
(42) Yasue, T.; Koyama, H.; Kato, T. *J. Vac. Sci. Technol. B* **1997**, *15*, 614.

(43) Liu, D.; Benstetter, G.; Frammelsberger, W. *Appl. Phys. Lett.* **2003**, *82*, 3898.
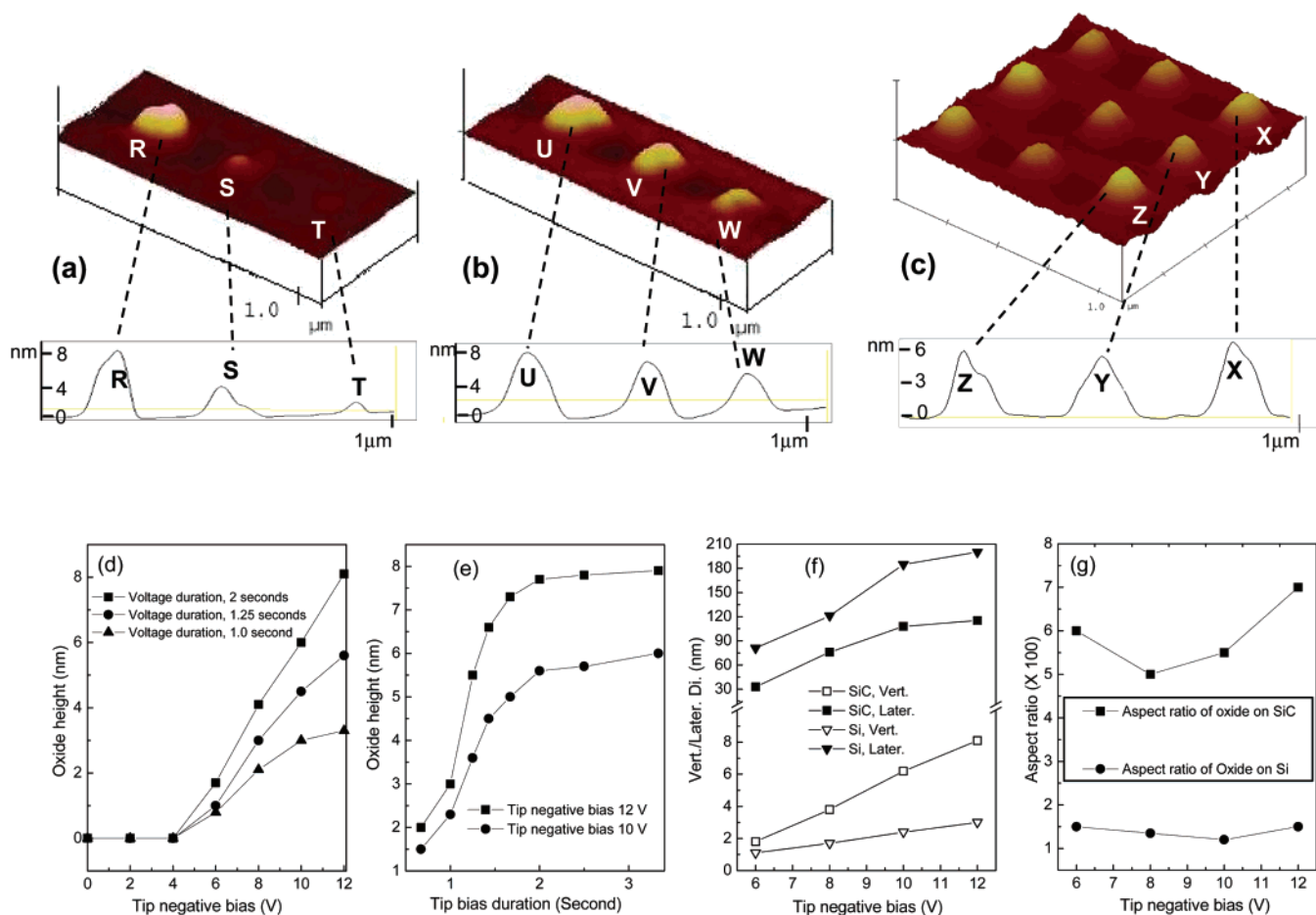
Figure 4. (a) Oxide dots R, S, and T grown with 12, 8, and 6 V negative tip biases, respectively. (b) Oxide dots U, V, and W grown at 2, 1.7, and 1.4 s bias duration. (c) 3 × 3 arrays of oxide dots grown with similar conditions. (d) and (e) Variation in oxide height versus bias voltage and bias duration. (f) Plots of vertical and lateral dimensions of oxide dots grown on SiC and Si surfaces under identical conditions. (g) Comparison of aspect ratio of AFM oxide grown on SiC and Si surfaces.

surfaces using identical conditions. Figure 4f shows the profiles of the vertical and lateral dimensions of oxide dots grown on SiC and Si surfaces at various negative biases. Figure 4g displays the aspect ratio (vertical versus lateral dimension) of oxides calculated from the data in Figure 4f for the two substrates. It is clear that the ratio of oxide on SiC is at least 4 times that of oxide grown on a Si surface under identical conditions. In the following paragraphs, we will address the possible reasons for the improved aspect ratio of AFM oxide on a SiC surface.

The aspect ratio of AFM oxide is rather a complicated issue. A few factors including (1) water meniscus, (2) surface stress, and (3) surface diffusion have been proposed to be responsible for it.[13-20] It is suggested that water meniscus spreads or defocuses the electrical field at the tip apex, giving rise to enhanced lateral growth of AFM oxide.[16,44] To clarify the influence of water on the electrical field, we simulated the electrical field distribution between the tip and surface with and without water meniscus. Figure 5a shows the configuration of the tip–surface system considered in the simulation. The tip radius of curvature, r, was assumed to be 20 nm, and the radius of water meniscus was varied between 20 and 200 nm. We applied a voltage magnitude of 10 V between the tip and surface. The tip–surface spacing, h, was taken as ≤1.0 nm, which is

typical in AFM oxidation. The simulation of electrostatic field distribution was carried out using a Maxwell 2D (SV) package which is based on the finite element method (ANSOFT Corporation). In Figure 5b, when there is no water meniscus between tip and surface (vacuum), the field (E) on the surface directly below the tip (position 0) reaches 10^{10} V/m. At positions of ±60 nm, the field decays by 2 orders of magnitude in a vacuum. The introduction of a water meniscus with $R = 20$ nm results in a decrease of E by one order at position 0, but the general distribution of E remains unchanged. When the radius of water meniscus is increased to $R = 60$ nm, E drops from 10^9 to below 10^6 V/m in the position range of 0 to ±60 nm and recovers to 10^8 V/m at positions outside the water meniscus. In other words, inside the water meniscus, E quickly decays by 3–4 orders of magnitude. Outside the meniscus, the field strength is the same as that in a vacuum. Similar results were calculated for the cases of $R = 100$ and 200 nm shown in Figure 5c. This observation indicates that the electrical field is "blocked" rather than "spread" by the water meniscus. Water is a dielectric, and its dielectrical constant is 78.4 at 25 °C and 1.0133×10^5 Nm^{-2}.[45] The presence of a dielectric will result in the decay of electrical field. On the other hand, water is also finitely conductive due to its ionization ($H_2O \rightarrow H^+ + OH^-$) and the presence of metallic ions in it. The conductivity of water

(44) Ph. Avouris, Martel, R.; Hertel, T.; Sandstrom, R. *Appl. Phys. A* **1998**, *66*, S659.

(45) Vaughan, W. E. *Digest Lit. Dielectr.* **1969**, *33*, 21–83.
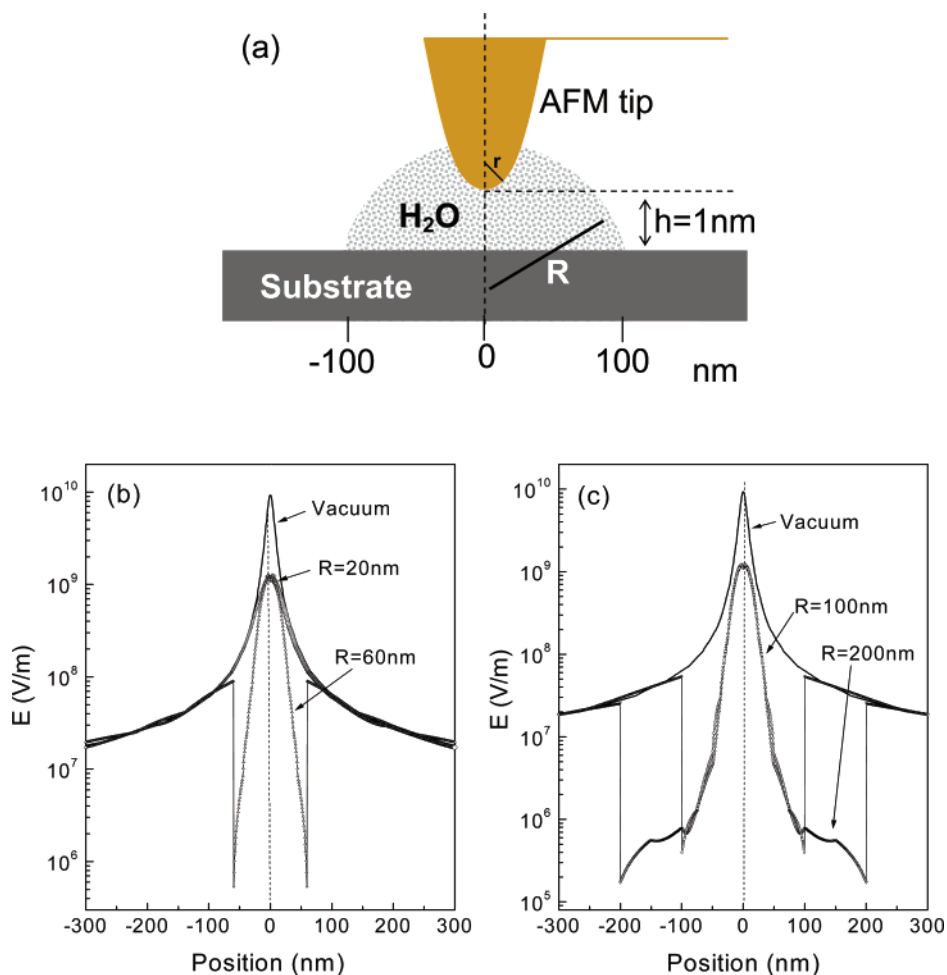
Figure 5. (a) The configuration of the tip/water/substrate model used in the simulation. (b) Simulated electrical field distribution for the models with vacuum, $R = 20$ nm and $R = 60$ nm water meniscus between AFM tip and substrate, respectively. (c) Simulated electrical field distribution for the models with vacuum, $R = 100$ nm and $R = 200$ nm water meniscus between AFM tip and substrate, respectively.

used in the above calculation is 0.01 S/m which is typical for pure water. When the conductivity is increased by 2 orders to 1.0 S/m, the calculated electrical field still maintains a distribution similar to that shown in Figure 5b,c for various R values. The simulation suggests that the water meniscus does not significantly affect the field distribution. Rather, the impact of water to AFM oxidation would be more related to chemistry, that is, water supplies the necessary oxidative species such as OH^- and O^- ions for the oxidation.
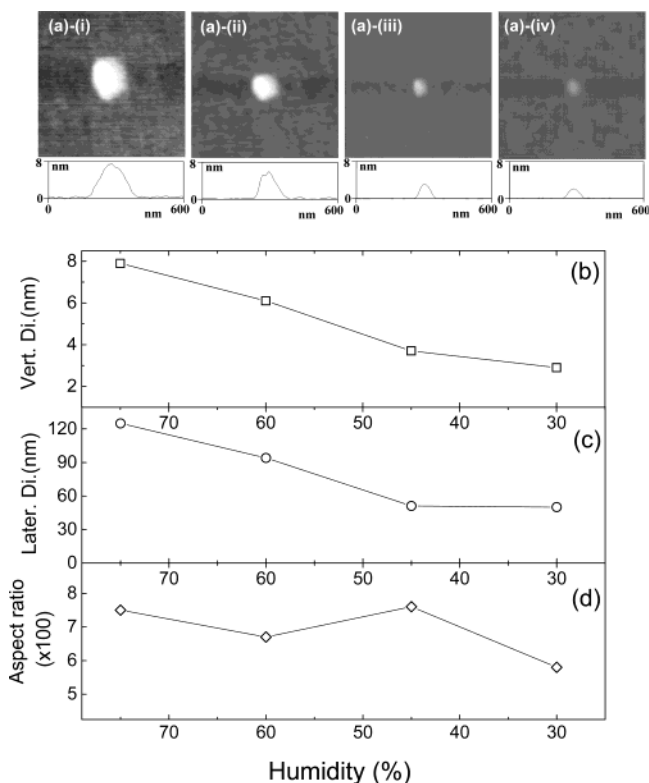
We further conducted AFM oxidation at various humidity conditions to examine the influence of water on oxide growth. A higher relative humidity usually corresponds to a larger water meniscus, although the detailed relationship between them is not clear. The humidity was experimentally controlled by gently heating the AFM tip−substrate system at different temperatures for different time durations using an external heating unit. A calibrated hegrometer was used to monitor the humidity. In this approach, the local humidity of the sample could be reduced to 30% from the ambient humidity of 75%. Figure 6a shows the 600×600 nm² AFM height images of oxide dots grown at a humidity of (i) 75%, (ii) 60%, (iii) 45%, and (iv) 30% while keeping all the other conditions identical. The vertical (height) and lateral (full width at half-maximum, fwhm) dimensions of these oxide dots were measured using AFM section analysis and plotted in Figure 6b and 6c, respectively. As shown in

Figure 6a−c, the dot oxide shows enhanced vertical and lateral growth at higher humidity. For example, the vertical and lateral dimensions of oxide grown at 75% humidity are 7.9 and 121 nm, respectively. In contrast, the corresponding dimensions for the oxide dot grown at 30% humidity are only 2.9 and 49 nm, respectively. The enhanced oxide growth at high humidity could be due to the increased water condensation at the tip apex, resulting in the formation of a bigger water meniscus between the tip and substrate. The observation in Figure 6 can be interpreted in terms of water meniscus size: a bigger water meniscus supplies more OH^- and O^- reactants for the AFM anodic reaction. The enriched oxidative species available at higher humidity facilitates the increase in both vertical and lateral oxide growth.

Surface stress develops due to the volume expansion of oxide relative to the substrate, and it is proportional to (V_{oxide} − $V_{substrate}$), where V_{oxide} and $V_{substrate}$ are the molecular volumes of oxide and substrate, respectively.[44,46] On the Si surface, the AFM oxide can be approximately considered to be SiO_2 ($V_{SiO_2} = 45$ A³). In the case of SiC surface, the formation of silicon oxycarbide (SiOC) should be taken into account, because carbon is most likely incorporated into the oxide during AFM oxidation as opposed to thermal oxidation wherein C could be liberated as CO or CO_2 via carbothermal reduction.[36,37] The
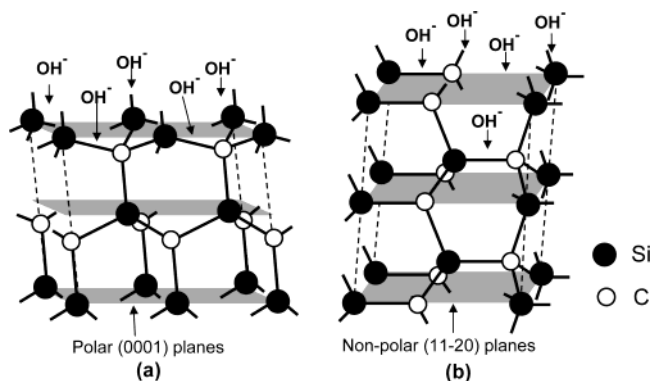
(46) Mott, N. F. *Philos. Mag. B* **1987**, *55*, 117.

Figure 7. (a) Vertical growth of AFM oxide involving OH$^-$ diffusion in the polar [0001] direction. (b) Lateral growth of AFM oxide involving OH$^-$ diffusion in the nonpolar directions such as [11$\bar{2}$0] axis.

Figure 6. Top: AFM height images of dot oxide grown at various humidity of (a)–(i) 75%, (a)–(ii) 60%, (a)–(iii) 45%, and (a)–(iv) 30%, respectively. Bottom: Plots of oxide (b) vertical dimension, (c) lateral dimension, and (d) aspect ratio as a function of humidity.

density of SiO$_2$ is 2.25 g/cm^3. If C is incorporated into SiO$_2$ to form SiOC, the density of the material will decrease. For example, at a C content of ∼20 atomic %, the density of SiOC is only 1.20 g/cm^3, which is almost half of the density of SiO$_2$.[47] At this C content, the molecular volume of SiOC, V_{SiOC}, is twice that of SiO$_2$. The molecular volumes of Si and SiC are ∼20 and ∼21 Å^3, respectively. The value of ($V_{SiOC} - V_{SiC}$) will increase as the C content increases. So, the overall effect of C incorporation is to induce greater surface stress and thus favor AFM oxide with low aspect ratio. Consequently, a lower oxide aspect ratio should be expected on SiC rather than the higher aspect ratio observed in Figure 4g. To account for this discrepancy, we considered the OH$^-$ lateral diffusion behavior on Si and SiC surfaces. On the Si surface, both the lateral and vertical oxide growth involve the diffusion of OH$^-$ along the nonpolar directions and insertion into Si–Si bonds. In contrast, on a SiC surface as shown in Figure 7, the vertical oxidation is associated to OH$^-$ diffusion in the polar [0001] axis and subsequent reaction with alternative Si and C layers on the (0001) planes. However, unlike the Si surface, the mechanism of lateral oxidation of SiC is quite different as shown in Figure 7b. It is governed by OH$^-$ diffusion in the nonpolar directions such as {11$\bar{2}$0} etc. which is perpendicular to the (0001) surface. In the {11$\bar{2}$0} direction, Si and C atoms coexist in the same plane, the content of each of them is 50%. OH$^-$ ions could react with both Si and C atoms to form oxide. Such a dependence of oxide growth on surface orientation and polarity has already been observed in the thermal oxidation of SiC. Shenoy et al. performed SiC thermal oxidation at 1150 °C in

wet oxygen, and they found that the oxide growth rate on a SiC (11$\bar{2}$0) surface is 3–5 times higher than that on a (0001) surface.[2] They ascribed the different oxidation rate to the effect of crystal orientation and anisotropy. Here in our AFM oxidation, the observed high aspect ratio could also be attributed to the intrinsic anisotropic OH$^-$ diffusion in polar and nonpolar directions such as the [0001] and [11$\bar{2}$0] axis. Such a difference in surface diffusion may be dominant in the AFM oxidation of SiC and counteract the effect of C incorporation. To confirm this, we compared the AFM oxides grown on both 6H-SiC (0001) and 4H-SiC (11$\bar{2}$0) surfaces. The (0001) and (11$\bar{2}$0) surfaces are quite different in their atomic structures and chemical compositions. For the (0001) surface, the Si atoms are arranged in hexagonal arrays with C_6 rotational symmetry. On the (11$\bar{2}$0) surface, however, both Si and C atoms are arranged into rectangular lattices. This structural difference can be seen clearly in the LEED (low-energy electron diffraction) patterns captured for the two surfaces as shown in Figures 8a and 8b. The hexagonal lattice pattern in Figure 8a is indicative of the C_6 symmetry present in the (0001) orientation, while the rectangular pattern in Figure 8b is characteristic of the (11$\bar{2}$0) surface unit cell. The AFM height images of oxide dots grown on the two surfaces under identical conditions are exhibited in Figures 8c and 8d, respectively. It is observed that the lateral dimensions of the oxide dots are similar on both surfaces, but the vertical dimension is systematically higher on the (11$\bar{2}$0) surface. This results in an ∼45% increase in oxide aspect ratio on the (11$\bar{2}$0) surface. Recently, M. Tello and R. García performed a comparative study of AFM oxidation in water (H$_2$O) and alcohol (CH$_3$CH$_2$OH) environments.[48] They observed that, for short tip bias pulses, AFM oxide generated in water shows a higher aspect ratio than that generated in alcohol. The authors attributed the difference in aspect ratio to the different mobility of oxyanions in water and alcohol. Here, the difference in polarity and chemical composition between the (0001) and (11$\bar{2}$0) surfaces would also cause distinct diffusion behavior of oxyanions and therefore lead to the improved oxide aspect ratio on the (11$\bar{2}$0) surface.

III. Dielectric Properties of AFM Oxide on the 6H-SiC (0001) Surface. The $I-V$ characteristics of dot oxide grown on SiC were recorded by contacting a Au-coated AFM tip with oxide to form a MOS structure. For such a structure, the electrical field reaches 10^7-10^8 V/cm and the $I-V$ curves are

(47) Kim, H. J.; Shao, Q.; Kim, Y.-H. *Surf. Coat. Technol.* **2003**, *171*, 39.

(48) Tello, M.; Garcia, R. *Appl. Phys. Lett.* **2003**, *83*, 2339.
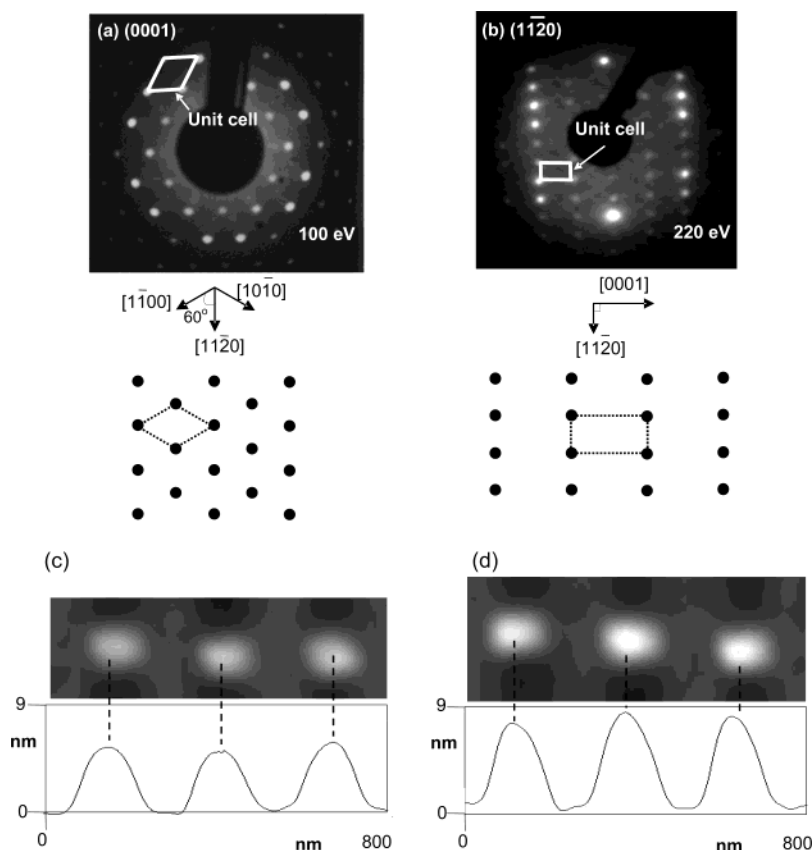
Figure 8. Top: LEED (low-energy electron diffraction) patterns and corresponding reciprocal lattice structures of SiC (a) (0001) and (b) (11$\bar{2}$0) surfaces. Bottom: AFM height images of oxide dots grown on (c) (0001) and (d) (11$\bar{2}$0) surfaces.

expected to obey the Fowler-Nordheim (F-N) law in the following format:[24,49]

$$J \propto \frac{V_{ox}^2}{\phi d_{ox}^2} \exp\left(-C\frac{d_{ox}}{V_{ox}}\phi^{3/2}\right)$$

where J is the current density, V_{ox} the voltage applied on oxide, ϕ the barrier height, d_{ox} the thickness of oxide, and C a fitting constant. The experimental and fitted $I-V$ characteristics are displayed in Figure 9a. The energy diagram of the Au/oxide/SiC MOS structure is also drawn in the inset of Figure 9a. The barrier height, ϕ, for the AFM oxide/SiC interface is derived from the best F-N fitting. It can be seen that the barrier height varies depending on the height of oxide. The ϕ values determined for 7.9, 4.3, and 1.2 nm thick oxides are 2.89, 2.67, and 2.54 eV, respectively. The value of 2.89 eV is quite close to that of 2.95 eV determined for thermal oxide on SiC.[7] X. Blasco et al. fabricated AFM oxide islands on a Si surface by scanning the tip across surface areas.[27] They found that the AFM oxide shows poorer dielectrical properties compared to thermal oxide, and they partially attributed this to the nondesired deposition of metal particles from the AFM tip. In our AFM oxidation, the tip was kept still at one point to grow an oxide dot; the incorporation of metal coatings from tip into the oxide is minimized. Thus, under optimized conditions, it is possible to grow AFM oxide on SiC with dielectrical properties compatible with that of thermal oxide.

The dielectrical stability of AFM oxides in terms of degradation and breakdown under electrical stress were further evaluated

by subjecting the oxide to repeated $I-V$ ramps. In Figure 9b, sudden current shooting events such as A and B in the $I-V$ curves were observed before dielectrical breakdown. After breakdown, the measured $I-V$ curve shows a much higher current level in the 0−4 V voltage range compared to that of the same oxide before breakdown (see Figure 9b). A similar current shooting event has been previously reported for thermal oxide on Si.[26] It is suggested that such a current shooting originates from the generation of defects and trapping/detrapping of individual charges in the generated traps. Electrostatic simulation showed that the release of captured elementary charges would lead to an increase of current in the same order of magnitude. We found that the current shooting is a random event: either single or multiple shooting could be observed on the $I-V$ curves. The samples which showed more shooting events were more prone to breakdown. The probability of current shooting and breakdown events strongly depends on the thickness of AFM oxide on SiC. In the experiments, the probability for the above events was estimated by performing $I-V$ ramps on AFM oxide until the breakdown $I-V$ characteristic was observed. The probability was then obtained by taking the percentage of the number of current shooting and breakdown events against the total number of $I-V$ ramps performed on the oxide. As shown in Figure 9c, the occurrence of both current shooting and breakdown events shows a monotonic decrease as the thickness of AFM oxide increases. The occurrence of current shooting and breakdown is around ∼16% and ∼10%, respectively, for the 7.9 nm thick oxide, while it is ∼32% and ∼25% for the 1.2 nm oxide. This observation is in good agreement with the results reported by S. Kremmer et al.[50] In

(49) Fowler, R. H.; Nordheim, L. *Proc. R. Soc. London, Ser. A* **1928**, *119*, 173.
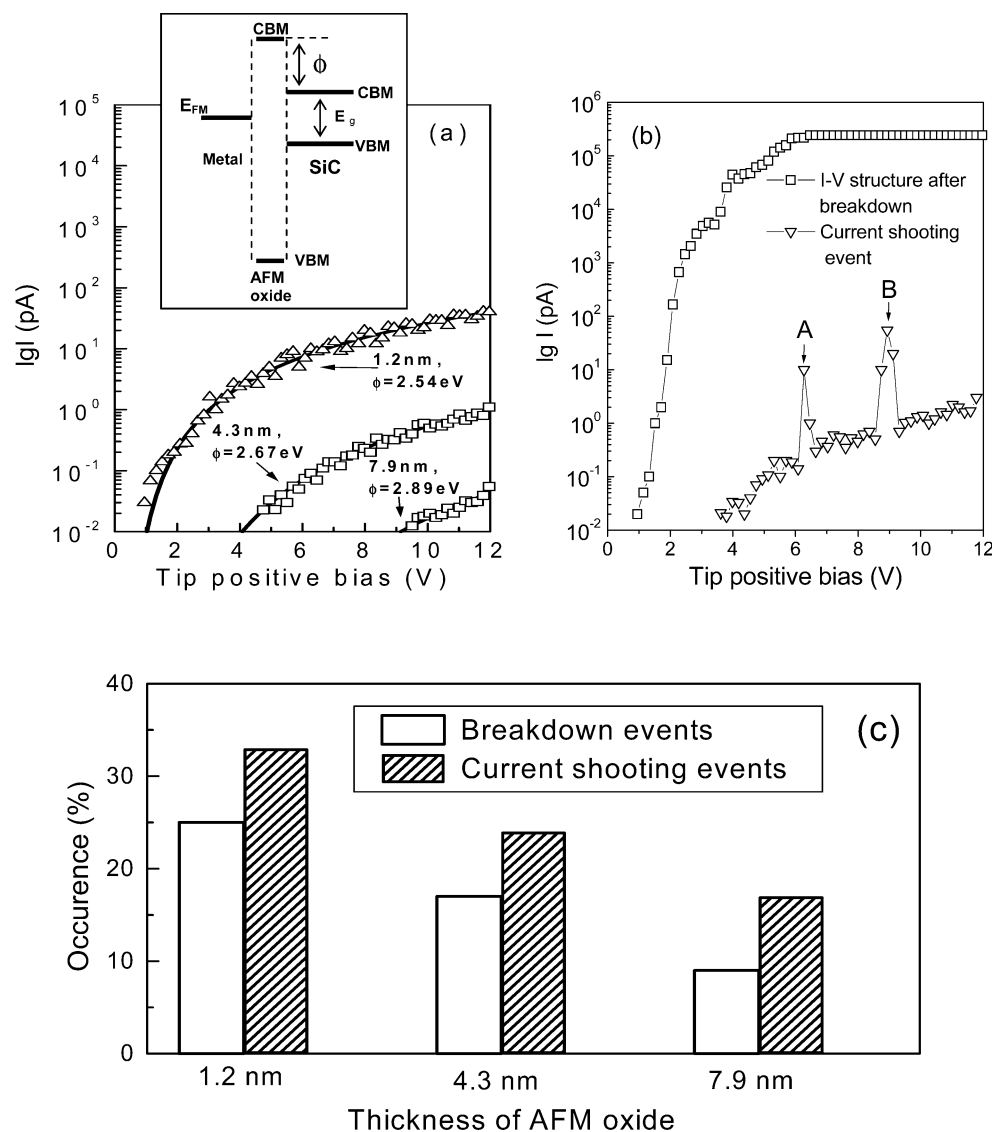
Figure 9. (a) $I-V$ characteristics recorded for AFM oxide with various thicknesses. Inset shows the energy diagram of the Au/oxide/substrate MOS structure. (b) Current shooting events and the $I-V$ curve recorded after dielectrical breakdown. (c) Comparison of the occurrence of current shooting and breakdown events among various AFM oxide on SiC.

their $I-V$ characterization of gate oxide using c-AFM, they found that the dielectrical breakdown voltage shifts to higher voltage with increased oxide thickness. It is believed that breakdown is closely related to the richness of defects which are randomly distributed in the oxide.[51,52] When the density of defects reaches a critical value, a conduction percolation path between the metal gate and semiconductor substrate is formed, leading to dielectrical breakdown in oxide. The AFM oxidation is performed in air, and the oxidative species are OH^- and O^- ions, etc. generated in the water meniscus. This renders AFM oxide more prone to defect formation as compared with thermal oxide which is grown in a vacuum. In addition, the possible formation of silicon oxycarbide in AFM oxide would also degrade its dielectric strength, as SiOC is considered as a low-k material.[47] The thinner AFM oxide with higher intrinsic defect density shows more current shooting events. It is also more subjected to the formation of extrinsic defects during electrical

stressing. As mentioned above, high tip voltage and long oxidation time favor a thick AFM oxide with a closed and dense structure. The low defect density of thicker AFM oxide accounts for its stronger dielectrical stability against degradation and breakdown.

Summary

We have observed, for the first time, the native oxide decomposition/etching and direct local oxide growth on a 6H-SiC (0001) surface induced by AFM probe oxidation. The native oxide decomposition was attributed to the field-emitted F-N current injected from the negatively biased AFM probe. This F-N current provides the activation energy for the native oxide decomposition on the SiC surface. Direct oxide growth on the SiC surface was achieved by immobilizing the AFM tip and increasing the oxidation time. The dependence of oxide height on the tip bias and oxidation time was discussed. In particular, under identical growth conditions, the aspect ratio of AFM oxide grown on SiC was found to be at least four times that on the Si surface. The improved aspect ratio was attributed to the anisotropic OH^- diffusion involved in vertical and lateral

(50) Kremmer, S.; Teichert, C.; Pischler, E.; Gold, H.; Kuchar, F.; Schatzmayr, M. *Surf. Interface Anal.* **2002**, *33*, 168.
(51) Stathis, J. H. *J. Appl. Phys.* **1999**, *86*, 5757.
(52) Dimaria, D. J.; Stathis, J. H. *Appl. Phys. Lett.* **1997**, *71*, 3230.

oxidation along polar and nonpolar directions such as the [0001] and [11$\bar{2}$0] axis in SiC crystal.

The dielectrical properties of AFM oxide grown on SiC was further investigated by $I-V$ characteristics. The barriers height, ϕ, of the AFM oxide/SiC interface was determined. The value of ϕ (2.54−2.89 eV) varies as a function of the thickness of AFM oxide: thicker oxide corresponds to higher barrier height. Current shooting events were observed on $I-V$ curves, which originate from the trap/release of charges in the defect sites. The occurrence of current shooting and breakdown events is closely related to the richness of defects in AFM oxide. Generally, thicker oxide grown under high tip bias and long oxidation time demonstrates better dielectrical strength against degradation and breakdown under electrical stress.